Journal of
Materials Chemistry A

ROYAL SOCIETY OF CHEMISTRY

9.8%-efficient and above 100 h-stable unassisted solar water splitting based on Si solar cells and photoelectrodes catalyzed by bifunctional Ni-Mo/Ni

Journal:	*Journal of Materials Chemistry A*
Manuscript ID	TA-ART-10-2018-010165.R1
Article Type:	Paper
Date Submitted by the Author:	27-Nov-2018
Complete List of Authors:	Fan, Ronglei; Soochow University; University of Michigan Cheng, Shaobo; McMaster University Huang, Guanping; Soochow University Wang, Yongjie; University of Michigan, Ann Arbor, Department of Electrical Engineering and Computer Engineering Zhang, Yazhou; University of Michigan; Xi'an Jiaotong University Vanka, Srinivas; University of Michigan Botton, Gianluigi; McMaster University Mi, Zetian; University of Michigan Shen, Mingrong; Soochow university,

SCHOLARONE™
Manuscripts

9.8%-efficient and above 100 h-stable unassisted solar water splitting based on Si solar cells and photoelectrodes catalyzed by bifunctional Ni-Mo/Ni

Ronglei Fan[a,b], Shaobo Cheng[c], Guanping Huang[a], Yongjie Wang[b], Yazhou Zhang[b,d], Srinivas Vanka[b], Gianluigi A. Botton[c], Zetian Mi[b,*] and Mingrong Shen[a,*]

[a]School of Physical Science and Technology, Jiangsu Key Laboratory of Thin Films, and Collaborative Innovation Center of Suzhou Nano Science and Technology, Soochow University, 1 Shizi street, Suzhou 215006, China.

[b]Department of Electrical Engineering and Computer Science, Center for Photonics and Multiscale Nanomaterials, University of Michigan, 1301 Beal Avenue, Ann Arbor, MI 48109, United States.

[c]Department of Materials Science and Engineering, Canadian Centre for Electron Microscopy, McMaster University, 1280 Main Street West, Hamilton, Ontario, L8S4M1, Canada.

[d]International Research Center for Renewable Energy, Xi'an Jiaotong University, 28 West Xianning Road, Xi'an 710049, China.

Abstract: Designing a highly efficient and stable photoelectrochemical (PEC) tandem cell for unassisted solar water splitting is considered as a promising approach for large-scale solar energy storage. To date, various tandem device configurations have been reported. However, the implementation of a solar-to-hydrogen conversion efficiency (η_{STH}) of 10% is still full of challenges, due to the incompatibility between the two photoelectrode materials. Here, we report a highly efficient and stable photovoltaic (PV)-PEC tandem device composed of a dual Si photoelectrode and two series-

connected ordinary Si PV cells. The dual-photoelectrode device consisting of an n^+np^+-Si photocathode and p^+pn^+-Si photoanode, which allow back illumination from the Si substrate, spatially and functionally decoupling the optical absorption and the catalytic activity. By further employing a Ni protective layer together with a bifunctional Ni-Mo catalyst for both Si photocathode and photoanode, the PV–PEC tandem cell can perform spontaneous water splitting without any applied bias. A high η_{STH} of 9.8 % with a stability of above 100 h was achieved in alkaline solution under parallel AM1.5G 1 sun illumination. This work essentially allows a modular independent optimization of each component which can enhance the efficiency and stability of the PV–PEC cells.

*Corresponding Author

Email: ztmi@umich.edu, Tel: 1 734 764 3963.

E-mail: mrshen@suda.edu.cn, Tel: 0086-0512-65112066.

Introduction

Unassisted solar water splitting, aided only by solar light, is becoming one of the most rapidly developed scientific fields since it is capable of converting and storing intermittent renewable solar energy into hydrogen using only renewable and clean resources.[1-5] Central to the essence of solar water splitting is the photovoltage. The thermodynamic potential required to split water into H_2 and O_2 is 1.23 V. However, a voltage above 1.8 V is required because of the transportation losses and overpotentials at both the cathode and anode.[6] Currently, there are two main methods to fulfill the photovoltage requirement for unassisted solar water splitting.[1] One is supplied by the photoexcited photoanode and/or photocathode in a photoelectrochemical (PEC) cell. The other is to use external photovoltaic (PV) module which is connected directly to the electrolyzer (EZ).

PEC cells, which have direct semiconductor/liquid contacts and simultaneous functions of light harvesting and electrolysis in a single device, are attractive because they avoid significant fabrication and system costs involved with the use of separated electrodes wired to solar cells.[7-10] To get the required photovoltage, tandem structure for solar light absorption is usually adapted, where the solar light is "eaten" firstly by one PEC electrode with wider bandgap, and the left enters into the other with narrower bandgap.[11] In some cases, the left solar light may also be designed to reach a rear photovoltaic device. Numerous semiconductors have currently been studied as photoelectrode materials such as $BiVO_4$, WO_3, Fe_2O_3 and GaN for PEC water splitting. For example, Shi *et al.* reported a solar-to-hydrogen efficiency (η_{STH}) of 7.1% achieved in a tandem cell coupling $BiVO_4/WO_3$ porous photoanodes fabricated on a distributed Bragg reflector with dye solar cells.[12] The limited efficiency is due to the difficulty to pair the two semiconductors which should have the close saturated photocurrent and work near the maximum energy output. To achieve a η_{STH} above 10% for commercial application, great efforts should be made to pair materials with appropriate bandgap energy, suitable band-edge positions, and sufficient photon harvesting for designing a highly efficient PEC cells.[13, 14]

In the PV–EZ mode, on the other hand, there is no such limitation. The PV devices absorb the solar light and supply energy to facilitate the reduction reaction at the cathode, and the oxidation reaction at the anode. The η_{STH} of the PV–EZ device is determined by the efficiency of PV and the H_2 and O_2 evolution overpotentials, which are influenced by the catalysts for hydrogen evolution reaction (HER) and oxygen evolution reaction (OER). Schüttauf et al. achieved a η_{STH} of 14.2% by using three bifacial Si heterojunction (SiHJ) cells and Ni foam electrocatalysts.[3] Using a perovskite tandem solar cell and a bifunctional earth-abundant NiFe catalyst, Luo et al. obtained a η_{STH} of 12.3%.[2] When four series-connected (SC) SiHJ solar cells are integrated to bifunctional NiFe inverse opal EZ, a η_{STH} of 9.54% has been reported recently.[4] Obviously, the PV–EZ mode has the advantage to achieve high η_{STH}, however, it is expensive because of the additional catalytic electrodes in EZ. Is there any possibility to combine the advantages of PEC and PV–EZ modes? In this work, we tried to replace the anode and cathode in the PV–EZ with a pair of photoelectrodes. We adapted Si photoanode and photocathode, which has similar saturated PEC photocurrents. They have recently been studied separately, since the former is favorable to work in alkaline electrolyte and the later in acid one. Great progresses have been achieved related to their efficiency and stability.[15-18] However, when working as a pair in alkaline solution, both the catalyst and protection layer to prevent the oxidation of Si surface have to be re-considered. Firstly, the catalyst integrated on the photoelectrodes should be both stable and efficient for HER and OER in basic solution. Such bifunctionality can prominently simplify the system and reduce costs.[19] Secondly, the protection layer between Si and catalyst should also be both stable for HER and OER. And thirdly, fast carrier transfer is required on the interfaces of the Si and alkaline solution.

Herein, we developed a Ni-Mo alloy by a facile electrodeposition method as efficient catalyst for both Ni-protected n^+np^+-Si photocathode and p^+pn^+-Si photoanode. When coupling with two SC ordinary Si PV cells, a PV–PEC system for unassisted solar water splitting is fulfilled. It has a few key features: (1) Ni-Mo alloy exhibits bifunctional catalytic activity for both HER and OER in alkaline solution; (2) 10 nm Ni

layer can protect both the Si photocathode and photoanode; (3) Ni is an efficient interfacial layer between Ni-Mo and Si, facilitating the transfer of carriers; (4) both photocathode and photoanode allow back illumination from the Si substrate, spatially and functionally decoupling the optical absorption and the catalytic activity. As a result, our PV–PEC water splitting cell generates an AM1.5 photocurrent density of 7.6 mA/cm^2 and a stability of above 100 h at zero bias under parallel illumination, achieving the highest η_{STH} of 9.8 % among the reported Si based PV–PEC tandem cells using only earth-abundant materials and ordinary solar cells. This provides a new and highly effective pathway towards efficient and low-cost solar water splitting devices.

Experimental section

Fabrication of n^{++}-Si Substrates, n$^+$np$^+$-Si and p$^+$pn$^+$-Si Solar Cells with MP Textured Surface

Highly doped n-type silicon (100) wafer (WRS Materials, two-inch double side polished, thickness: 256–306 μm; resistivity: < 0.005 Ω·cm), n-type Si (100) wafer and p-type Si (100) (WRS Materials, two-inch double side polished, thickness: 256–306 μm; resistivity: 1–10 Ω·cm) were used for this work. The MP textured surface was produced on both sides of above three types of Si by chemical etching in a potassium hydroxide solution (1.8% KOH in weight with 20% IPA in volume) for 30 minutes at 78 °C. Residual KOH on the surface was neutralized by hydrochloric acid (HCl, 20% in volume), cleaned by acetone/methanol and then native oxide was removed by hydrofluoric acid (HF, 10% in volume).

For the fabrication of n$^+$np$^+$-Si and p$^+$pn$^+$-Si PV cells, n-Si and p-Si with MP textured surface were first covered with liquid phosphorus and boron dopant precursor by spin coating, respectively (Futurrex, Inc.). Subsequently, the thermal diffusion process was conducted at 950 °C for 180 min under a N$_2$ flow rate of 500 standard cubic center meter per minute (sccm) in a diffusion furnace. The thermal diffusion process leads to the formation of an n$^+$ emitter layer and a p$^+$ electron back reflection layer for

p-Si based solar cells and a p^+ emitter layer and an n^+ hole back reflection layer for n-Si based solar cells, respectively. The remnant of the precursor was removed in buffered oxide etch solution (BOE with a 6:1 volume ratio of 40% NH_4F to 49% HF in aqueous solution) for 10 mins. Then the wafers were rinsed in deionized water and dried under a stream of N_2.

Metal Films Deposition

Before metal deposition, Si electrodes were etched in BOE solution for 30 s to remove the surface native oxide layer again. Ni or Ti films were sequentially deposited on n^{++}-Si, n^+np^+-Si and p^+pn^+-Si via E-beam evaporation at a deposition rate of 0.5 Å/s, followed by an annealing at 550 °C for 2 mins. The film thickness of ~10 nm was measured using TEM.

Catalyst Deposition

The Ni-Mo catalyst was deposited using an electrodeposition recipe, which was similar to the one has been described previously in another report.[20] Prior to the electrodeposition, the Si electrodes were etched in BOE solution for 30 s to remove any native surface oxides. Similar to the n^{++}-Si and Ni/n^{++}-Si electrodes, the surface of Ni/n^+np^+-Si and Ni/p^+pn^+-Si photoelectrodes were also sufficiently conductive that they behaved like metals in the precursor solution. Therefore, they are used as the working electrode for the electrodeposition of Ni-Mo catalyst, which was carried out in a three-electrode cell configuration, using the Si as working electrode, an Ag/AgCl (3M KCl) as reference electrode, and a Ni wire as counter electrode. The electrodeposition bath consisted of an aqueous solution of 325 g/L $Ni(SO_3NH_2)$ (hydrate, crystalline, Alfa Aesar), 30 g/L H_3BO_3 (>99.5%, Aldrich), and 5 g/L $NaMoO_4$ (> 98%, Aldrich). Finally, the pH was adjusted to 4.0 with KOH (95–97%, Merck). The precursor solution was purged by nitrogen for 30 min before deposition. The electrodeposition of Ni-Mo catalyst on the Si surface was performed for 30–180 s at a cathodic current density of -25 mA/cm^2, producing 750–4500 mC/cm^2 of cathodic charge density.

Structural Characterization

The surface morphology was analyzed by a Field-Emission SEM (SU8000, Hitachi). STEM images and EELS elemental mapping were taken by a FEI Titan TEM operated at 200 kV. The lattice fringes of Ni-Mo, Ni and Si were analyzed by a software named as DigitalMicrograph. XPS measurements were performed at room temperature using a spectrometer hemispherical analyzer (ESCALAB 250Xi, Thermo).

Electrochemical Catalytic Activity Measurements

The OER and HER catalytic activity measurements were performed using an electrochemical workstation (BioLogic, SP-150) without solar simulation, with a Ni wire as the counter electrode and Ag/AgCl (3M KCl) as the reference electrode. The electrolyte of all the measurements was 1 M KOH electrolyte solution (pH=13.6), which was purged by nitrogen for 30 min. The final potential was translated into the RHE according to the following equation:

$$E(RHE) = E(Ag/AgCl) + 0.059\,V \times pH \qquad (1)$$

where $E(Ag/AgCl) = 0.197\,V$. LSV measurements were performed at room temperature, with a scan rate of 10 mV/s. The voltage sweep ranges for OER and HER were 1.2–1.7 V_{RHE} and 0 to -0.6 V_{RHE}, respectively. The LSV data were corrected for any uncompensated resistance losses. The Tafel slopes of different samples stemmed from their corresponding LSV curves. The Tafel slope can be calculated by the Tafel equation ($V_{op} = b\log(J) + a$, where J, V_{op}, and b represent the current density, overpotential, and Tafel slope, respectively). EIS was performed when the working electrode was biased at a constant potential of -0.1 V_{RHE} and 1.3 V_{RHE} under dark in a frequency range from 1 Hz to 100 kHz with an AC amplitude of 10 mV. To evaluate the stability of different electrodes, long-term J–t measurements were conducted at constant potential with a current density of -10 mA/cm^2 and 10 mA/cm^2 for HER and OER in 1 M KOH electrolyte solution. The electrolyte was replaced and the sample was rinsed every 12 h during the stability measurements.

PEC Measurements

PEC measurements of the single Si photocathode and photoanode were conducted in a three-electrode cell configuration with a Si photoelectrode as working electrode, an Ag/AgCl (3M KCl) as reference electrode and a Ni wire as counter electrode. A solar simulator (Newport Oriel) with an AM 1.5G filter was used as the light source, and the light intensity was calibrated to be 100 mW/cm^2 at the position of the photoelectrode for all PEC experiments. The PEC experiments including LSV and J–t tests were performed using an electrochemical workstation (BioLogic). The performance of the photoelectrodes was measured using the LSV curves at 10 mV/s at room temperature. The ABPE of single Si photocathode and photoanode was calculated from the corresponding LSV curves using equation (2) and (3), respectively.

$$\text{ABPE} = \left[\frac{|J\ (mA/cm^2)| \times V_{bias}\ (V)}{100\ (mW/cm^2)}\right] \times 100\ \% \tag{2}$$

$$\text{ABPE} = \left[\frac{J\ (mA/cm^2) \times (1.23 - V_{bias})\ (V)}{100\ (mW/cm^2)}\right] \times 100\ \% \tag{3}$$

where J is the photocurrent density, and V$_{bias}$ is the applied bias divided from the corresponding LSV curves.

Two-electrode measurements were conducted by connecting the working electrode lead of the potentiostat to the Ni-Mo/Ni/p$^+$pn$^+$-Si photoanode and the reference and counter electrode lead of the potentiostat to the Ni-Mo/Ni/n$^+$np$^+$-Si photocathode. In order to fulfill unassisted solar water splitting, two series-connected ordinary Si solar cells were added into the Si photoanode/Si photocathode system, called as PV–PEC system. On the other hand, the system consists of two Ni-Mo/Ni/n^{++}-Si electrode and four series-connected ordinary Si solar cells was called PV–EZ. The evolved H$_2$ gas was carried out in a two-electrode cell and sampled using an air tight syringe and analyzed by a gas chromatVograph (Shimadzu GC-8A) equipped with a thermal conductivity detector and Argon carrier gas. The η$_{STH}$ was calculated according to equation (4):

$$\eta_{STH} = \left[\frac{\eta_F \times J_{op}\ (mA/cm^2) \times 1.23\ V}{100\ (mW/cm^2)}\right] \times 100\ \% \tag{4}$$

where η_F is the Faradic efficiency and J_{op} is the current density at zero bias.

Results and discussion

n^{++}-Si substrates with micro-pyramid (MP) textured surface were firstly fabricated to improve the density of catalytic active sites, according to the procedure in the Experimental section. Then a thin Ni film via electron beam (E-beam) evaporation was fabricated on the MP Si surface (denoted as Ni/n^{++}-Si), and Ni-Mo catalyst was finally deposited on the top of Ni/n^{++}-Si by electrodeposition (denoted as Ni-Mo/Ni/n^{++}-Si). The surface scanning electron microscope (SEM) pictures of Ni-Mo catalyst deposited for 90 s on Ni/n^{++}-Si was presented in Fig. 1a. The Ni-Mo catalyst is visible in the form of particles coated homogenously on the surface of the electrode, consistent with previously reported literatures.[20, 21] In Fig. 1b, the surface of Ni/n^{++}-Si uniformly covered by Ni-Mo particles can be observed on a large scale. Taking a closer look, the mean diameter of Ni-Mo particles is about 50 nm (Fig. S1†). Ni-Mo catalyst was also deposited directly on the MP textured Si surface (denoted as Ni-Mo/n^{++}-Si) as shown in Fig. S2†. The schematic overview of the electrodeposition setup of Ni-Mo catalyst was demonstrated in Fig. S3†. For comparison, the SEM picture of Ni/n^{++}-Si demonstrates a thin and dense Ni film with a uniform morphology (Fig. S4†). The SEM pictures of MP textured Si surface with and without the deposition of Ni-Mo catalyst for 90 s were presented in Fig. S4b† and Fig. S4c†, indicating that inserting an interfacial Ni buffer layer would not change the morphology of Ni-Mo catalyst. The cross-sectional characterization of the as-synthesized Ni-Mo/Ni/n^{++}-Si electrode was performed using a high angle annular dark field scanning transmission electron microscope (HAADF-STEM). Illustrated in Fig. 1c, Ni-Mo catalyst in the form of particles with a diameter of about 50 nm is observed on the surface of Ni/n^{++}-Si, consistent with the SEM observation in Fig. 1a. Fig. 1d is the corresponding high-resolution STEM (HR-STEM) picture of Ni-Mo/Ni interfaces. The interplanar spacings of particles on the top resolved by TEM is around 0.206 nm, corresponding to the (111) plane of Ni-Mo; while the interplanar spacings of the thin film is about 0.217 nm,

corresponding to the (002) plane of Ni. The interfaces could be observed more clearer in Fig. S5†. Note that the lattice fringes of Ni-Mo catalyst were not as clear as the lattice fringes of Si substrate, suggesting the low crystallinity of the thin film layer. Electron energy loss spectroscopy (EELS) elemental mapping was carried out to identify the distribution of Si, Ni, Mo, and O elements in the as-prepared sample. As illustrated in Fig. 1e, the uniform distribution of Ni and Mo elements in Ni-Mo catalyst supports its alloy structure. It is also observed that a uniformly distributed Ni layer with a thickness of about 10 nm was successfully fabricated on the interface of Si and Ni-Mo catalyst.

The surface chemical composition of the Ni-Mo catalyst was further unveiled by X-ray photoelectron spectroscopy (XPS). In Fig. 1f, two peaks appear at the binding energy (BE) of 852.8 and 870.1 eV in Ni 2p spectrum, representing Ni^0 $2p_{3/2}$ and Ni^0 $2p_{1/2}$, respectively; while the two peaks located at 855.8 and 873.7 eV are originated from +2 oxidation state of Ni 2p orbitals, confirming the existence of Ni^{2+} in the layer surface as can be seen in Fig. 1e. Fig. 1g is for the Mo 3d region. The peaks at the BE of 228.0 and 231.2 eV represent Mo^0 $3d_{5/2}$ and Mo^0 $3d_{3/2}$, respectively; while the other two peaks at 229.3 and 233.2 eV can be observed, corresponding to +4 oxidation state of Mo 3d. Such results confirm the formation of Ni-Mo catalyst as previously reported.[22-24] Furthermore, the atomic ratio of Mo to Ni is about 3: 17 according to the atomic states of Ni^0 (Ni^0 $2p_{3/2}$ and Ni^0 $2p_{1/2}$) and Mo^0 (Mo^0 $3d_{5/2}$ and Mo^0 $3d_{3/2}$) (Table S1†). By integrating all the characterization results together, Ni-Mo alloy particles on Ni-protected Si electrode was well-designed. As will be demonstrated below, such a Ni-Mo/Ni/Si can be an efficient and stable structure for both HER and OER.
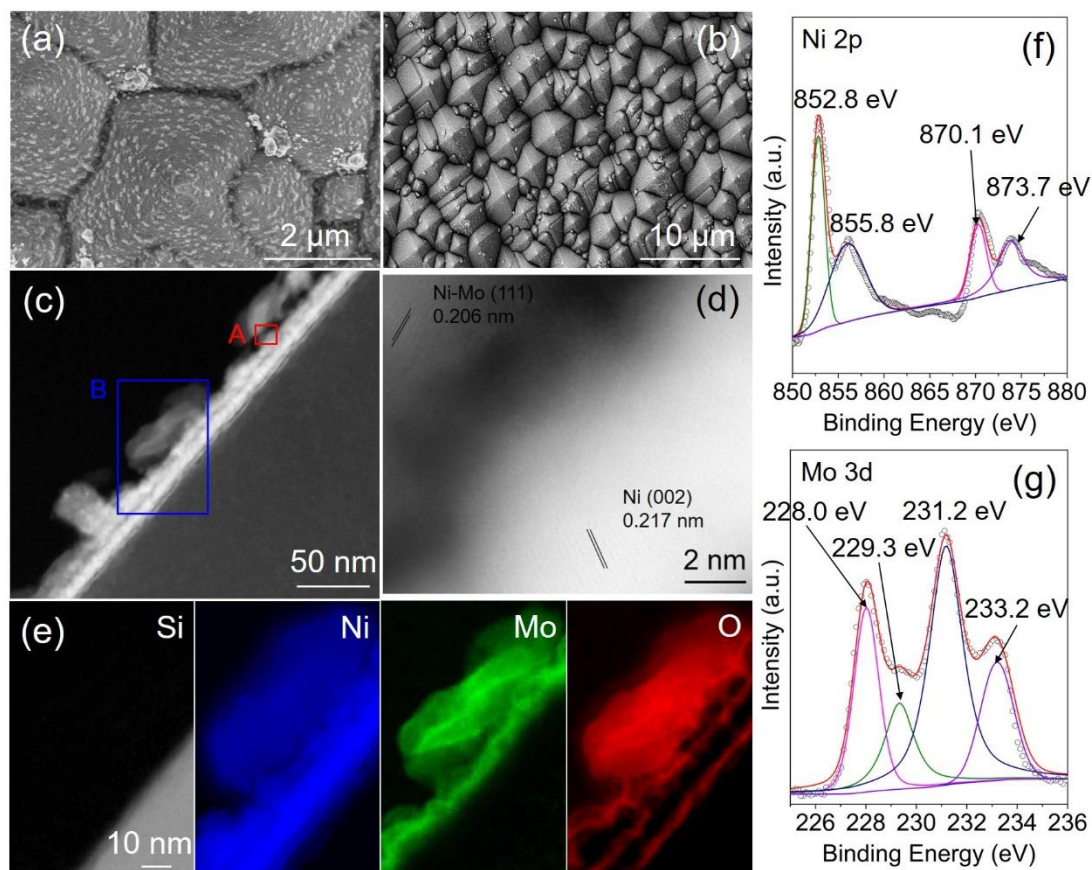
Fig. 1. Microscopic characterization of as-prepared Ni-Mo/Ni/n^{++}-Si electrode. (a) Surface SEM images of Ni-Mo particles supported on Ni/n^{++}-Si electrode. (b) Lower magnification SEM images of Ni-Mo particles supported on Ni/n^{++}-Si electrode. (c) Cross-sectional HAADF-STEM image of as-synthesized Ni-Mo/Ni/n^{++}-Si electrode. (d) A typical HR-TEM image taken from the selected area A in (c). (e) EELS elemental mapping result for the selected area B in (c). The Si K, Ni L$_{2,3}$, Mo M$_{4,5}$, O K edges are selected for the mapping. High-resolution XPS of (f) Ni 2p and (g) Mo 3d in Ni-Mo/Ni/n^{++}-Si electrode.

The electrocatalytic activities of the n^{++}-Si substrates with Ni, Ni-Mo and Ni-Mo/Ni toward HER and OER were evaluated in a 1.0 M KOH solution with a standard three-electrode system. We firstly present the data for the HER. For comparison, the blank n^{++}-Si substrate was used in the control experiment. Linear sweep voltammetry (LSV) curves in Fig. 2a reveal significant variations in the HER activities of the different electrocatalysts. As expected, the blank n^{++}-Si substrate exhibits a very limited

HER activity, while Ni-Mo/n^{++}-Si exhibits remarkable catalytic activities toward HER, with a low overpotential of 0.19 V at -10 mA/cm^2. The optimal loading amount of Ni-Mo catalyst on n^{++}-Si for HER electrocatalytic performance can be found in Fig. S6†. The electrocatalytic activity observed herein for Ni-Mo on n^{++}-Si is very close to the case for the previously reported Ni-Mo on planar p$^+$-Si electrode for HER in a pH 4.5 buffer solution.[25] Although Ni-Mo catalyst has been reported as an excellently electrocatalytic activities with sufficiently long-term stability under HER conditions,[26] the surface of Si still needs to be protected under alkaline conditions. Our group has recently demonstrated that an inserted Ti buffer layer can protect Si surface and reduce resistances of charge transfer on the electrode/electrolyte interface in a solution containing HClO$_4$.[27] Thus we also investigate the role of 10 nm Ti in the present study. The insertion of Ti buffer layer between Ni-Mo catalyst and n^{++}-Si substrate exhibits a slightly better activity than the Ni-Mo/n^{++}-Si. An overpotential of 0.17 V is required to afford a current density of -10 mA/cm^2 (Fig. S7a† and Fig. S7b†). Unfortunately, the long-term stability of Ni-Mo/Ti/n^{++}-Si electrode is far from satisfactory. The current density decreased from -10 mA/cm^2 to -7 mA/cm^2 after 12 h of continuous electrochemical H$_2$ evolution (Fig. S7c†). The reason of this decay is ascribed to the instability of Ti/n^{++}-Si surface under alkaline conditions (Fig. S7d† and Fig. S7e†). Recently, Ni has been regarded as a very promising bifunctional electrocatalytic activity and stability toward HER and OER under alkaline conditions, due to its low cost, high elemental abundance, high corrosion resistance and high electrical conductivity.[28] Ni alone shows a relatively slower HER kinetics than Ni-Mo catalyst, with an overpotential of 0.28 V at -10 mA/cm^2 (Fig. 2a). However, the HER activity can be dramatically enhanced by depositing Ni-Mo onto Ni.[29] By optimizing the loading amount of Ni-Mo catalyst on Ni/n^{++}-Si, the Ni-Mo/Ni/n^{++}-Si electrode can achieve a current density of -10 mA/cm^2 at an overpotential of 0.12 V (Fig. 2a and Fig. S6b†). The insertion of a thin Ni can fill the interparticle gap of Ni-Mo catalyst that will subsequently increase the number of HER active sites, and therefore allow more electrons to transfer across the entire surface. Such low overpotential by Ni-Mo/Ni

catalyst is comparable to the noble metal Pt under alkaline conditions.[22, 30] Fig. 2b displays the corresponding Tafel plots to characterize the catalytic kinetic of various electrocatalysts. The Tafel slope signifies how much potential is needed to achieve a tenfold current density, which should be ideally small.[31] The Tafel slope of Ni-Mo/Ni/n^{++}-Si substrate (48 mV/dec) is significantly lower than that of Ni-Mo/n^{++}-Si (56 mV/dec) and Ni/n^{++}-Si (88 mV/dec), suggesting favorable HER kinetics on Ni-Mo/Ni/n^{++}-Si electrode.

Electrochemical impedance spectroscopy (EIS) was applied to provide further insights into the catalytic kinetics on various electrocatalysts. The EIS was conducted at -0.1 V *vs.* reversible hydrogen electrode (V_{RHE}) and the resulting Nyquist plots are presented in (Fig. S8†) and fitted with an equivalent circuit model (Fig. S9†) to extract the charge transfer resistance (R_{ct}) from n^{++}-Si to electrolyte through the catalyst. The small R_{ct} value of 12.7 Ω for the Ni-Mo/Ni/n^{++}-Si electrode is comparable to 10.4 Ω for the Pt/n^{++}-Si electrode, and significantly lower than 30.1 Ω of the Ni-Mo/n^{++}-Si, 129.8 Ω of the Ni/n^{++}-Si. This illustrates that the most efficient electron transfer happens between the Ni-Mo/Ni/n^{++}-Si and electrolyte during HER operation.

In addition to a high catalytic activity, long-term catalytic durability is also a major concern for large-scale practical applications. Chronoamperometric J–t tests for Ni/n^{++}-Si and Ni-Mo/Ni/n^{++}-Si electrodes are conducted at a constant potential to achieve a current density of -10 mA/cm^2 (Fig. 2c). Both the Ni/n^{++}-Si and Ni-Mo/Ni/n^{++}-Si electrodes show an outstanding long-term stability after over 100 h continuous HER operation. Obviously, the conformal Ni layer on n^{++}-Si surface can work as the efficient protective layer to connect Si and catalyst, furthermore, Ni-Mo catalyst itself is not deactivated during HER operation under alkaline condition. The comparison of the LSV curves of the Ni/n^{++}-Si and Ni-Mo/Ni/n^{++}-Si electrodes before and after the stability measurements coincide with their original ones, further conforming the salient catalytic stability (as shown in the inset of Fig. 2c).

The present Ni-Mo/Ni is not only an outstanding HER catalyst, but also an excellent OER catalyst. The electrocatalytic OER performances of Ni-Mo/Ni along

with Ni-Mo and Ni was evaluated by LSV curves with the identical electrolyte solution and electrode configuration to HER (Fig. 2d). By careful optimization of the loading amount of Ni-Mo catalyst on n^{++}-Si and Ni/n^{++}-Si electrodes, the Ni-Mo/Ni/n^{++}-Si electrode exhibits an excellent OER activity with an ultralow overpotential of 0.25 V at 10 mA/cm^2, which is much lower than 0.29 V of the Ni-Mo/n^{++}-Si and 0.42 V of the Ni/n^{++}-Si (Fig. S10†). We next examine the OER kinetics based on the corresponding Tafel plots (Fig. 2e). Ni-Mo/Ni/n^{++}-Si electrode displays the lowest Tafel slope of 50 mV/dec, much superior to those of Ni-Mo/n^{++}-Si (62 mV/dec) and Ni/n^{++}-Si electrode (95 mV/dec). To further investigate the OER kinetic characteristics of the three electrodes, EIS was conducted at 1.3 V_{RHE} by using same electrochemical experimental conditions and fitted with an equivalent circuit model same as the one used for the HER. The Ni-Mo/Ni/n^{++}-Si electrode again shows the smallest R_{ct} value of 8.5 Ω among all the tested electrodes (37.3 Ω for Ni-Mo/n^{++}-Si and 99.7 Ω for Ni/n^{++}-Si) (Fig. S11†). This lowest value suggests rapid charge transfer in the Ni-Mo/Ni/n^{++}-Si electrode, thereby promoting a high OER activity. To evaluate the long-term stability of Ni/n^{++}-Si and Ni-Mo/Ni/n^{++}-Si electrodes toward OER, J–t tests with above 100 h continuous OER operation are conducted (Fig. 2f). Ni/n^{++}-Si shows a slight increase in current density, from 10 to 10.5 mA/cm^2, which is attributed to the oxidation of the Ni surface to the NiO$_x$ or Ni(OH)$_2$.[32] Furthermore, the slight increase of current density is also observed for Ni-Mo/Ni/n^{++}-Si electrode, signaling the excellent durability of the Ni-Mo/Ni/n^{++}-Si electrode for OER catalysis. The chemical composition of this sample was analyzed by XPS (Fig. S12†). The spectra of both Ni 2p and Mo 3d reveal that the peaks of Ni^0 and Mo^0 are disappeared, while +2 oxidation state of Ni 2p and +6 oxidation state of Mo 3d are dominated, indicating the oxidation of Ni-Mo catalyst after 100 h continuous OER operation. Such oxidation of catalyst is normal and the surface oxide may become active center for OER.[33] These results reveal that the Ni-Mo/Ni layer possesses a great potential as a bifunctional electrocatalyst for electrolytic or PEC water splitting.
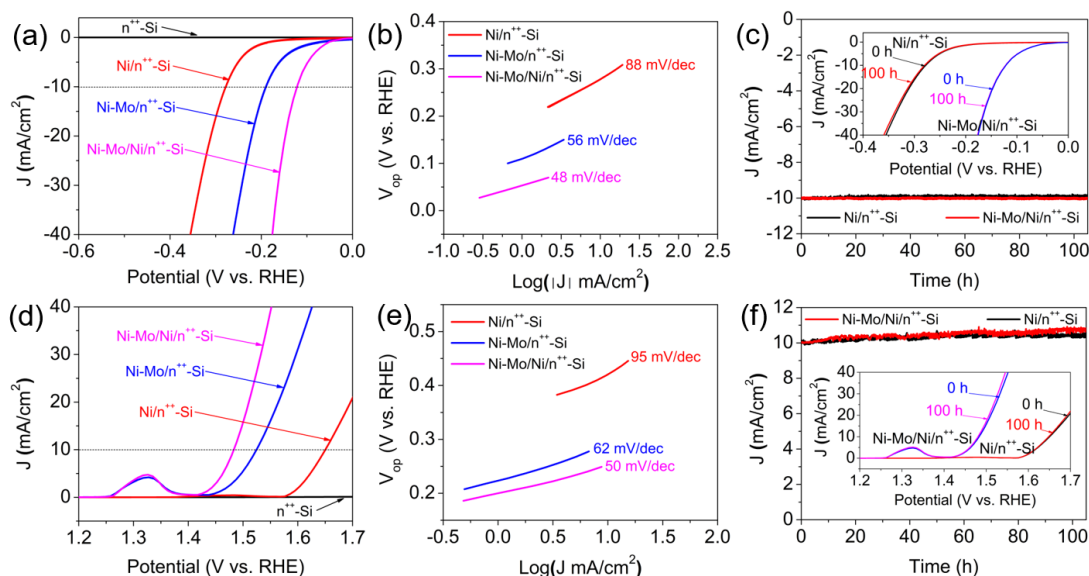
Fig. 2. HER and OER electrocatalytic performance of various catalysts. (a), (d) LSV curves in 1 M KOH. (b), (e) Corresponding Tafel plots derived from the LSV curves presented in (a) and (d). (c), (f) The J–t tests for the Ni/n^{++}-Si and Ni-Mo/Ni/n^{++}-Si electrodes at a constant potential of -0.28 and -0.2 V$_{RHE}$ for HER, and 1.65 and 1.48 V$_{RHE}$ for OER over 100 h of continuous operation, respectively.

With the acquired bifunctional electrocatalysts in hand, we try to integrate them on Si photocathodes and photoanodes to evaluate their PEC performance by recording the LSV curves in 1 M KOH solution (pH=13.6) in the dark and under AM1.5G 1 sun illumination (100 mW/cm^2), respectively. The onset potential (V$_{on}$) is defined as the potential which drives a photocurrent density to -1 mA/cm^2 for photocathode and 1 mA/cm^2 for photoanode from the LSV curves. p-Type based Si with a n$^+$ frontal emitter and an additional p$^+$ layer on the back of n$^+$p Si is a popular structure used as photocathode, where catalysts are loaded on the n$^+$ layer in order to improve the HER kinetics and onset potential.[34, 35] Fig. 3a shows the LSV curves of n$^+$pp$^+$-Si photocathodes with and without various catalysts. The set-up is schematically represented in (Fig. S13a†). No current is observed for all the electrodes under dark conditions. Bare n$^+$pp$^+$-Si photocathode can only produce H$_2$ at a large overpotential under illumination, and its photocurrent density increases gradually from -1 to -36.8 mA/cm^2 with applied potential changes from about -0.2 to -1.0 V$_{RHE}$ (Fig. S14†). This

exemplifies a catalyst is needed for HER. The LSV curve right-shifts obviously after the adding of 10 nm Ni, with a V_{on} of 0.2 V_{RHE} and a J_0 of -12.5 mA/cm^2 (J_0: photocurrent density at 0 V_{RHE} for photocathodes). Despite the enhancement in PEC performance, the J_s (saturated photocurrent density) for 10 nm Ni coated n^+pp^+-Si reduces significantly from -36.8 to -23 mA/cm^2 when compared with the pure n^+pp^+-Si. In order to eliminate the interference from other factors, such as electrolyte composition, bubble formation or contact resistances, n^+pp^+-Si with and without the coating of 10 nm Ni are fabricated as solid-state Si PV cells. The LSV curves of various solid-state n^+pp^+-Si PV cells shown in (Fig. S15†) exhibit similar J_s compared with that in Fig. 3a. Furthermore, after 10 nm Ni is coated on a transparent glass, the specimen becomes darker (Fig. S16†). The UV-vis absorption spectra of glass substrates with and without the decoration of 10 nm Ni film clearly show that 10 nm Ni film has absorption in the 300-900 nm wavelength region (Fig. S17a†). By integrating the UV−Vis absorption spectra of the calculated 10 nm Ni film with the standard solar spectrum of AM 1.5G, a integrated photocurrent density of 13.0 mA/cm^2 was obtained (Fig. S17b†), which is close to the difference in J_s (13.8 mA/cm^2) between bare n^+pp^+-Si and 10 nm Ni coated n^+pp^+-Si measured in Fig. S15†. These results confirm that the decrease in J_s is due to the parasitic light absorption by the 10 nm Ni, since the J_s of Si is proportional to the light intensity absorbed by Si. The PEC performance of Ni/n^+pp^+-Si photocathode can be enhanced by depositing Ni-Mo onto Ni. Its J_0 increases from -15 to -20 mA/cm^2, V_{on} further right-shifts from 0.2 to 0.35 V_{RHE} and the maximum applied bias photon-to-current efficiency (ABPE) increases from 0.6 % to 3.28 %, although its J_s decreases from -23 to -20 mA/cm^2 (Table S2†). We note that the HER activity of Ni-Mo/Ni can be comparable to that of Pt under alkaline conditions as we discussed above. However, the maximum ABPE of Ni-Mo/Ni/n^+pp^+-Si photocathode is limited by the insufficient absorption by Si. Therefore, alternative strategies should be put forward to further improve the maximum ABPE of Ni-Mo/Ni based Si photocathode.

Compared to p-Si based solar cells, n-Si based solar cells possess a key advantage: a much higher carrier lifetime as well as a much better lifetime stability under

illumination.[36, 37] Most importantly, it allows light illumination from the rear side of the device, while the protective layer and catalysts at the front side can be sufficiently thick for designing more efficient and stable photocathode without concerning about any light shielding issues.[38] Fig. 3b shows the LSV curves of n^+np^+-Si photocathodes integrated with the same amount of catalysts as used in n^+pp^+-Si photocathodes. The set-up is schematically represented in (Fig. S13b†). Both photocathode and solid-state PV cell of the bare n^+np^+-Si exhibit slightly better performance than those of the corresponding n^+pp^+-Si (Fig. S14† and Fig. S15†). Significantly, compared with Ni-Mo/Ni/n^+pp^+-Si, the V_{on} of Ni-Mo/Ni/n^+np^+-Si right-shifts from 0.4 to 0.5 V_{RHE}, while its J_0 increases obviously from -20.3 to -36.3 mA/cm^2, due to the spatial and functional decoupling of optical absorption and catalytic activity for the Si photocathode. Furthermore, the maximum ABPE of the Ni-Mo/Ni/n^+np^+-Si photocathode is 6.9% (Table S2†), which is superior to most of the previously reported Si photocathodes coated with earth-abundant catalysts (Fig. 3d, Table S3†). Note that the highest ABPE (10.1 %) for HER in alkaline electrolyte was obtained by a spatioselectively etched SiN$_x$ layer on n^+p-Si microwire arrays coupled with spatioselective NiSi and Ni-Mo, however, this structure is complicated and not cost-effective.[39]

In addition to HER performance, Ni-Mo/Ni is also a moderate OER catalyst as we mentioned above. In Fig. 3c, the PEC OER performance of the Ni-Mo/Ni/p^+pn^+-Si photoanode along with the Ni/p^+pn^+-Si and bare p^+pn^+-Si photoanodes, were evaluated by LSV curves using the set-up represented in (Fig. S13c†). No current is observed for all the photoanodes under dark conditions. The bare p^+pn^+-Si photoanode exhibits a negligible photocurrent under illumination, suggesting that Si photoanode is prone to be oxidized quickly when in contact with an electrolyte under anodic conditions.[40] The coating of Ni and Ni-Mo/Ni on the p^+pn^+-Si photoanode surface can improve the PEC OER performance obviously. Conceivably, the Ni-Mo/Ni/p^+pn^+-Si photoanode exhibits the best performance: a V_{on} of 0.94 V_{RHE}, a J_0 of 34.5 mA/cm^2 and a maximum ABPE of 3.11% (Table S2†). This value of maximum ABPE is much close to the highest ABPE (3.3%) among the previously reported Si based photoanodes (Fig. 3e and Table S4†).

Note that the highest ABPE of 3.3% obtained by np^+-Si/SiO$_x$/NiFe photoanode was achieved with iR-compensation, and the actual value of maximum ABPE was hard to know.[41]

To better understand the evidently enhanced PEC performance of both Si photocathodes and photoanodes, EIS measurements were performed to elucidate the charge transfer resistances in the different photoelectrodes. Nyquist plots fitted with two different equivalent circuit models show large $R_{ct,1}$ for both bare Si photocathode (1510.1 Ω) and photoanode (1895.2 Ω), suggesting the sluggish charge transfer kinetics from Si to electrolyte. $R_{ct,2}$ represents the charge-transfer resistance from the Ni or Ni-Mo catalyst to the electrolyte. The total value of resistance ($R_{ct,1}$ + $R_{ct,2}$) radically decreases to 98.3, 73.3, 131.6 and 77.5 Ω for Ni/n^+np^+-Si, Ni-Mo/Ni/n^+np^+-Si, Ni/p^+pn^+-Si and Ni-Mo/Ni/p^+pn^+-Si, respectively (Fig. S18† and Table S5†). The significantly diminished resistance after the loading of Ni-Mo/Ni catalyst indicates that the uniformly Ni-Mo/Ni decoration on the surface of Si acts as an effective mediator, which greatly accelerates the charge transfer kinetics between illuminated Si and electrolyte for both HER and OER. The excellent performance of Ni-Mo/Ni/n^+np^+-Si photocathode and Ni-Mo/Ni/p^+pn^+-Si photoanode can be attributed to the highly electrocatalytic activity of bifunctional Ni-Mo/Ni catalyst, the high current density under back illumination without compromising Si light absorption and the fast charge transfer kinetics at the Si/electrolyte interface.
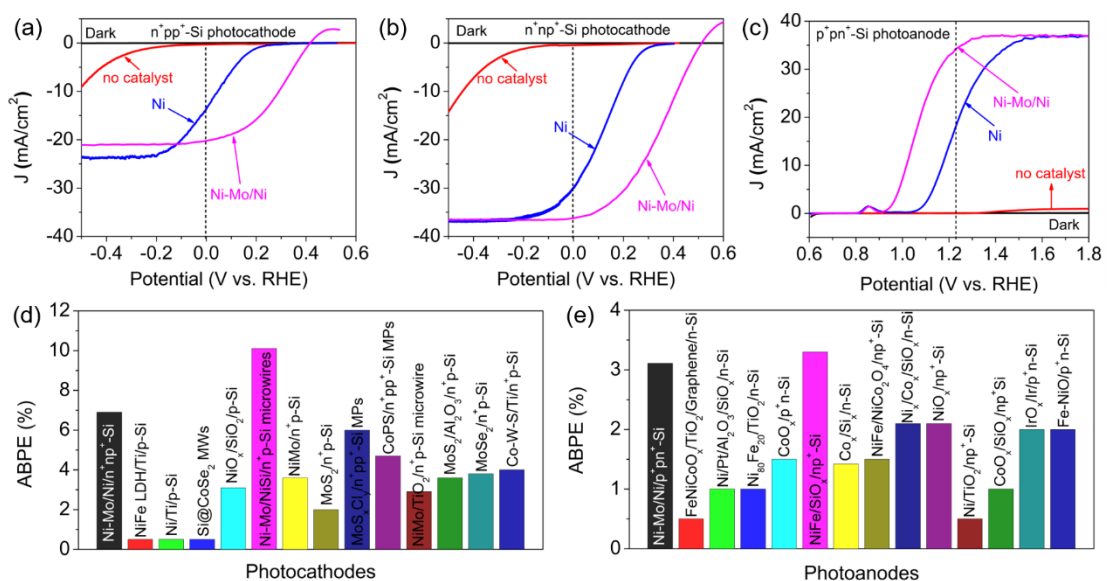
Fig. 3. PEC performance of single Si photoelectrode. LSV curves of (a) n^+pp^+-Si photocathodes, (b) n^+np^+-Si photocathodes and (c) p^+pn^+-Si photoanodes integrated with and without various catalysts. (d) Comparison of the maximum ABPE among various state-of-the-art Si photocathodes coated with earth-abundant catalysts. (e) Comparison of the maximum ABPE among various state-of-the-art Si based photoanodes.

As mentioned in the introduction, Si photoanode and photocathode have recently been studied intensively by using a three-electrode configuration separately. However, the performance of the dual-Si photoelectrode consisting of a Ni-Mo/Ni/n^+np^+-Si photocathode and Ni-Mo/Ni/p^+pn^+-Si photoanode has rarely been evaluated using a two-electrode configuration in a fully functioning solar-to-hydrogen device. In order to demonstrate the potential for unassisted solar-driven water splitting, a PV–PEC combined system is designed for unassisted solar-driven water splitting, where the dual-Si photoelectrode and 2 SC Si PV cells are under parallel illumination (Fig. 4a). Firstly, the LSV curves of the dual-Si photoelectrode and the 2 SC Si PV cells were evaluated independently, which are recorded in a two-electrode configuration under dark and AM1.5G 1 sun illumination conditions, as shown in Fig. 4b. The sample areas of dual-Si photoelectrodes and the 2 SC Si PV cells are both controlled to be 0.5 cm^2, due to the current matching requirement. Details of the 2 SC Si PV cells is shown in Fig. S19†. By the current at which two LSV curves cross, the theoretical η_{STH} of PV–PEC combined system can be estimated to be 9.73 %, according to the following equation: $\eta_{STH} = 1.23\,V \times J_{op}(mA/cm^2)/100\,mW/cm^2$. The actual LSV curves and the corresponding η_{STH} of the PV–PEC combined system are also conducted. As shown in Fig. 4c, a J_{op} of 7.97 mA/cm^2 is achieved under a zero bias condition and the practical η_{STH} can be obtained as 9.80 %. The Faradaic efficiency (η_F) of this system is 100 % (Fig. S20†), indicating the true water splitting happens. Fig. 4d shows the long-term J–t test and corresponding η_{STH} of the PV–PEC system under AM1.5G 1 sun illumination at zero bias. A stable photocurrent density of 7.97 mA/cm^2 is achieved, which indeed

corresponds to the working point of Fig. 4c. The η_{STH} stays invariant even after continuous unassisted solar water splitting for 100 h under AM1.5G 1 sun illumination. Note that the slight variation of ~ 0.24 % in η_{STH} can be attributed to the generation and release of bubbles on the surface of dual-Si photoelectrode. In order to achieve a high η_{STH} of PV–PEC system, it is especially important to pair the PV and PEC components which should have the close saturated photocurrent and work near the maximum energy output. As a result, the value of η_{STH} and stability of our Si-based PV–PEC system is among the best when comparing with the previously reported PV–PEC configuration (Table S6†). For comparison, the performance of unassisted water splitting for the PV–EZ system consisting of Ni-Mo/Ni/n^{++}-Si EZs and 4 SC Si PV cells was also conducted (Fig. S21†). The η_{STH} of PV–EZ system (9.3 %) here is slightly lower compared to some Si-based PV–EZ systems already reported (Table S7†). We attribute the difference in η_{STH} mainly to the lower efficiency of Si PV cells and catalytic activity of catalysts on EZs. Typically, a η_{STH} of 14.2% was achieved by Schüttauf *et al.*, in which a highly efficient Si heterojunction (SiHJ) PV cells with an efficiency of 20.6% and a Fill Factor of 0.832, and the most efficient noble metal Pt, IrO$_x$ electrocatalysts on Ni foam were used.[3] The SiHJ PV cell is capable of producing a high V$_{oc}$ of above 700 mV under AM1.5G 1 sun illumination.[4] We believe that the η_{STH} of our PV–PEC system can be further enhanced by coupling the SiHJ based photoelectrodes and SiHJ PV cells into the combined system.
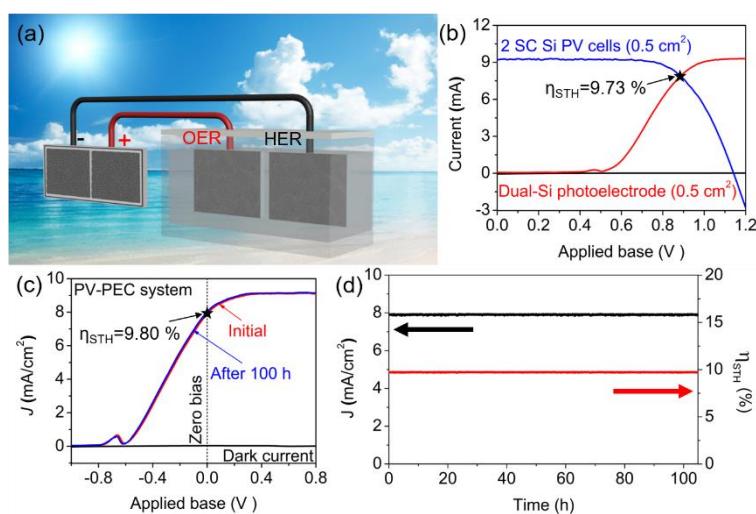

Fig. 4. Unassisted water splitting by using the combination of a dual-Si photoelectrode

and 2 SC Si PV cells. (a) Schematic illustration of the combined PV–PEC system. (b) Two-electrode LSV curves of the dual-Si photoelectrode under dark (black) and AM1.5G 1 sun illumination conditions (red). Also shown are the LSV curves of 2 SC Si PV cells under AM1.5G 1 sun illumination (blue). Estimated η_{STH} for the combined PV–PEC system is marked on the crossing point. (c) Two-electrode LSV curves of the combined PV–PEC system before and after over 100 h continuous unassisted solar water splitting. (d) Long-term J–t test and the corresponding η_{STH} for the combined PV–PEC system during continuous unassisted solar water splitting for over 100 h.

Conclusion

In conclusion, we demonstrated the fabrication and characterization of a highly efficient and stable PV–PEC tandem cell, consisting of a Ni-Mo/Ni/n^+np^+-Si photocathode, a Ni-Mo/Ni/p^+pn^+-Si photoanode and two Si PV cells, for overall solar water splitting in basic solution. The bifunctional Ni-Mo catalyst prepared using a facile electrodeposition method exhibits highly electrocatalytic activity for both HER and OER. A 10 nm Ni acts as not only an excellent protective layer for Si, but also an efficient interfacial layer between Ni-Mo and Si. In addition, the rear p-n junction structure of Si photocathode and photoanode is constructed to decouple the optical absorption and the catalytic activity spatially and functionally, so the Ni-Mo/Ni layer can be sufficiently thick for devising more efficient and stable photoelectrodes without concerning about the light shielding issues. Finally, by careful optimization of each component, the PV–PEC tandem cell achieved a spontaneous water splitting for more than 100 h with a η_{STH} of 9.8% under parallel AM1.5G 1 sun illumination.

Acknowledgements

References:

1. K. Zhang, M. Ma, P. Li, D. H. Wang and J. H. Park, *Adv. Energy Mater.*, 2016, **6**, 1600602.

2. U. De Silva, J. Masud, N. Zhang, Y. Hong, W. P. R. Liyanage, M. Asle Zaeem and M. Nath, *J. Mater. Chem. A*, 2018, **6**, 7608-7622.

3. J.-W. Schüttauf, M. A. Modestino, E. Chinello, D. Lambelet, A. Delfino, D. Dominé, A. Faes, M. Despeisse, J. Bailat, D. Psaltis, C. Moser and C. Ballif, *J. Electrochem. Soc.*, 2016, **163**, F1177-F1181.

4. H. Song, S. Oh, H. Yoon, K.-H. Kim, S. Ryu and J. Oh, *Nano Energy*, 2017, **42**, 1-7.

5. M. G. Kibria, F. A. Chowdhury, S. Zhao, B. AlOtaibi, M. L. Trudeau, H. Guo and Z. Mi, *Nat. Commun.*, 2015, **6**, 6797.

6. M. G. Walter, E. L. Warren, J. R. McKone, S. W. Boettcher, Q. Mi, E. A. Santori and N. S. Lewis, *Chem. Rev.*, 2010, **110**, 6446-6473.

7. J. A. Turner, *Science*, 1999, **285**, 687-689.

8. K. Zhang, S. Ravishankar, M. Ma, G. Veerappan, J. Bisquert, F. Fabregat-Santiago and J. H. Park, *Adv. Energy Mater.*, 2017, **7**, 1600923.

9. B. Jin, E. Jung, M. Ma, S. Kim, K. Zhang, J. I. Kim, Y. Son and J. H. Park, *J. Mater. Chem. A*, 2018, **6**, 2585-2592.

10. Z. Jiao, X. Guan, M. Wang, Q. Wang, B. Xu, Y. Bi and X. S. Zhao, *Chem. Eng. J.*, 2019, **356**, 781-790.

11. J. W. Jang, C. Du, Y. Ye, Y. Lin, X. Yao, J. Thorne, E. Liu, G. McMahon, J. Zhu,

A. Javey, J. Guo and D. Wang, *Nat. Commun.*, 2015, **6**, 7447.

12. X. Shi, H. Jeong, S. J. Oh, M. Ma, K. Zhang, J. Kwon, I. T. Choi, I. Y. Choi, H. K. Kim, J. K. Kim and J. H. Park, *Nat. Commun.*, 2016, **7**, 11943.

13. C. Ding, W. Qin, N. Wang, G. Liu, Z. Wang, P. Yan, J. Shi and C. Li, *Phys. Chem. Chem. Phys.*, 2014, **16**, 15608-15614.

14. B. AlOtaibi, S. Fan, S. Vanka, M. G. Kibria and Z. Mi, *Nano Lett.*, 2015, **15**, 6821-6828.

15. S. W. Boettcher, E. L. Warren, M. C. Putnam, E. A. Santori, D. Turner-Evans, M. D. Kelzenberg, M. G. Walter, J. R. McKone, B. S. Brunschwig, H. A. Atwater and N. S. Lewis, *J. Am. Chem. Soc.*, 2011, **133**, 1216-1219.

16. R. Fan, W. Dong, L. Fang, F. Zheng and M. Shen, *J. Mater. Chem. A*, 2017, **5**, 18744-18751.

17. M. J. Kenney, M. Gong, Y. Li, J. Z. Wu, J. Feng, M. Lanza and H. Dai, *Science*, 2013, **342**, 836-840.

18. M. R. Shaner, S. Hu, K. Sun and N. S. Lewis, *Energy Environ. Sci.*, 2015, **8**, 203-207.

19. W. Lu, T. Liu, L. Xie, C. Tang, D. Liu, S. Hao, F. Qu, G. Du, Y. Ma, A. M. Asiri and X. Sun, *Small*, 2017, **13**, 1700805.

20. E. L. Warren, J. R. McKone, H. A. Atwater, H. B. Gray and N. S. Lewis, *Energy Environ. Sci.*, 2012, **5**, 9653-9661.

21. W. Vijselaar, P. Westerik, J. Veerbeek, R. M. Tiggelaar, E. Berenschot, N. R. Tas, H. Gardeniers and J. Huskens, *Nat. Energy*, 2018, **3**, 185-192.

22. Q. Zhang, P. Li, D. Zhou, Z. Chang, Y. Kuang and X. Sun, *Small*, 2017, **13**, 1701648.

23. J. Zhang, T. Wang, P. Liu, Z. Liao, S. Liu, X. Zhuang, M. Chen, E. Zschech and X. Feng, *Nat. Commun.*, 2017, **8**, 15437.

24. Q. Yao, Z.-H. Lu, W. Huang, X. Chen and J. Zhu, *J. Mater. Chem. A*, 2016, **4**, 8579-8583.

25. J. R. McKone, E. L. Warren, M. J. Bierman, S. W. Boettcher, B. S. Brunschwig,

N. S. Lewis and H. B. Gray, *Energy Environ. Sci.*, 2011, **4**, 3573-3583.

26.   C. C. McCrory, S. Jung, I. M. Ferrer, S. M. Chatman, J. C. Peters and T. F. Jaramillo, *J. Am. Chem. Soc.*, 2015, **137**, 4347-4357.

27.   R. Fan, G. Huang, Y. Wang, Z. Mi and M. Shen, *Appl. Catal. B: Environ.*, 2018, **237**, 158-165.

28.   V. Vij, S. Sultan, A. M. Harzandi, A. Meena, J. N. Tiwari, W.-G. Lee, T. Yoon and K. S. Kim, *ACS Catal.*, 2017, **7**, 7196-7225.

29.   I. A. Digdaya, P. P. Rodriguez, M. Ma, G. W. P. Adhyaksa, E. C. Garnett, A. H. M. Smets and W. A. Smith, *J. Mater. Chem. A*, 2016, **4**, 6842-6852.

30.   Y. Wang, G. Zhang, W. Xu, P. Wan, Z. Lu, Y. Li and X. Sun, *ChemElectroChem*, 2014, **1**, 1138-1144.

31.   F. Yu, H. Zhou, Y. Huang, J. Sun, F. Qin, J. Bao, W. A. Goddard, 3rd, S. Chen and Z. Ren, *Nat. Commun.*, 2018, **9**, 2551.

32.   I. A. Digdaya, G. W. P. Adhyaksa, B. J. Trzesniewski, E. C. Garnett and W. A. Smith, *Nat. Commun.*, 2017, **8**, 15968.

33.   R. Subbaraman, D. Tripkovic, K. C. Chang, D. Strmcnik, A. P. Paulikas, P. Hirunsit, M. Chan, J. Greeley, V. Stamenkovic and N. M. Markovic, *Nat. Mater.*, 2012, **11**, 550-557.

34.   Q. Ding, J. Zhai, M. Caban-Acevedo, M. J. Shearer, L. Li, H. C. Chang, M. L. Tsai, D. Ma, X. Zhang, R. J. Hamers, J. H. He and S. Jin, *Adv. Mater.*, 2015, **27**, 6511-6518.

35.   R. Fan, W. Dong, L. Fang, F. Zheng, X. Su, S. Zou, J. Huang, X. Wang and M. Shen, *Appl. Phys. Lett.*, 2015, **106**, 013902.

36.   D. L. Meier, H. P. Davis, R. A. Garcia, J. Salami, A. Rohatgi, A. Ebong and P. Doshi, *Solar Energy Mater. Solar Cells*, 2001, **65**, 621-627.

37.   R. Fan, J. Min, Y. Li, X. Su, S. Zou, X. Wang and M. Shen, *Appl. Phys. Lett.*, 2015, **106**, 213901.

38.   Y. Wan, S. K. Karuturi, C. Samundsett, J. Bullock, M. Hettick, D. Yan, J. Peng, P. R. Narangari, S. Mokkapati, H. H. Tan, C. Jagadish, A. Javey and A. Cuevas,

ACS Energy Lett., 2018, **3**, 125-131.

39.   W. Vijselaar, R. M. Tiggelaar, H. Gardeniers and J. Huskens, *ACS Energy Lett.*, 2018, **3**, 1086-1092.

40.   D. Bae, B. Seger, P. C. Vesborg, O. Hansen and I. Chorkendorff, *Chem. Soc. Rev.*, 2017, **46**, 1933-1954.

41.   X. Yu, P. Yang, S. Chen, M. Zhang and G. Shi, *Adv. Energy Mater.*, 2017, **7**, 1601805.

Table of Contents

9.8%-efficient and above 100 h-stable unassisted solar water splitting based on Si solar cells and photoelectrodes catalyzed by bifunctional Ni-Mo/Ni